A Co-Additives Strategy for Blocking Ionic Mobility in Methylammonium-Free Perovskite Solar Cells and High Stability Achievement.

Daming Zheng, Tao Zhu, Thierry Pauporté*

Chimie ParisTech, PSL Research University, CNRS, Institut de Recherche de Chimie Paris (IRCP), UMR8247, 11 rue P. et M. Curie, F-75005 Paris, France
* Author for the correspondence. E-mail: thierry.pauporte@chimieparisrech.psl.eu
Website: www.pauportegroup.com

Abstract

The present work describes the synthesis of methylammonium-free and bromide-free $Cs_xFA_{1-x}PbI_3$ (FA for formamidinium) perovskite photovoltaic layers with intrinsic outstanding properties in terms of crystallinity, defect waiving/passivation and ionic mobility blocking by using a co-additives approach. It consists in mixing two chloride additives in the perovskite precursor solution: potassium chloride and ammonium chloride. KCl favors the PbI_2 precursor solubilization and results in purer perovskite phase. NH_4Cl allows the control of the crystallization growth speed, leads to the formation of large crystal grains and well-crystallized layers. By the glow-discharge optical emission spectroscopy (GD-OES) technique, we have been able to directly visualize that potassium incorporated in the whole film blocks the iodide mobility by defect passivation. We have also clearly correlated the reduction (or suppression) of iodide mobility and the reduction (or suppression) of the *J-V* curve hysteresis. We have found that blocking the ionic mobility is insufficient to fully stabilize the halide perovskite material which also requires the crystallization monitoring performed in parallel by the second additive. It resulted in $Cs_{0.1}FA_{0.9}PbI_3$ cells with a stabilized PCE at 20.02% and with superior stability.

Keywords: Methylammonium-free perovskite solar cells; ammonium chloride and potassium chloride additives; glow-discharge optical emission spectroscopy; iodide mobility blocking; Hysteresis suppression.

1. Introduction

During the last decade, organo-metal halide perovskites (PVKs) have risen as the most promising semiconductor family for photovoltaic solar cells due to a broad range of unique properties. They are prepared from solutions, at low temperature and at low cost. They present long charges carriers diffusion lengths that favor their collection at the contacts, low exciton binding energy in the case of the 3D compounds that favors the charge separation and a direct optical transition [1-19]. Moreover, their optical bandgap can be tuned by playing on the material composition and can approach the Schockley-Queisser limit for the maximum power conversion efficiency (PCE) [9]. As a result of the recent research efforts from the international scientific community, they now reach a certified record PCE of 25.5% [13]. It places this technology as the most efficient of the thin films ones and close to the best crystalline silicon performances. However, this idyllic picture must be moderated by the present stability concerns of these devices. The preparation of stable and efficient PSCs remains the main challenge for the future of this technology and a promising approach is the chemical engineering of the perovskite precursor solution (PPS). In these solutions, two kinds of components are added: (i) the elements and compounds that will form the film and (ii) those that will be eliminated during the synthesis, especially in the final layer-annealing step. By working on this chemistry and on the crystallization control, it is possible to dramatically increase the material stability, not only by reaching the intrinsic entropic stabilization, but also by enhancing the crystallinity, suppressing defect formation, and stabilizing grain boundaries.

Methylammonium (MA)-based PSCs are able to reach very high efficiency, however, the presence of MA is a source of material instability and devices' rapid failure since this compound decomposes with heating, outgases with time and is hygroscopic [9]. We have shown recently that it is possible to stabilize $FA_{1-x}MA_xPbI_3$ perovskite with a minimum of MA by using methylammonium chloride as an additive and in a large amount in the precursor deposition solution. It leads to the formation of pure α-phase perovskite films with large grains due to the presence of chloride ion [18,19]. However, the full elimination of MA^+ must be targeted for a better stabilization [20-33]. The most popular approach for methylammonium-free PSCs consists in replacing MA^+ by Cs^+ and/or by Rb^+ cations, two alkali metals [20,21,31-33]. Several authors have developed interfacial engineering for boosting the performances of

the devices.[22-24, 33] However, in the absence of methylammonium, PSCs usually show inferior PCEs due to an insufficient quality of the PVK material. Increasing the material crystallinity and passivating defects must be targeted [31]. Prochowicz et al.[25] employed an excess of CsCl in FAPbI$_3$ PPS to get high quality perovskite films. Gao et al.[26] also used CsCl mixed with CsI in the PPS with the presence of bromide and achieved a stabilized PCE of 20.5%. Recently, Zhang et al.[27] proposed to assist the fast crystallization of the layer by employing formamidine containing antisolvent. By this method they regulated the nucleation and improved the crystallization of (Rb,Cs,FA)PbI$_3$ films. Our approach has been to use a mixture of KCl and NH$_4$Cl as co-additives to mediate the PVK film growth. KCl has been mainly reported for the treatment of the ETL surface, especially of SnO$_2$ and NiO$_x$ layers, before the growth of the PVK layer by spin-coating [34-38]. Potassium doping of MAPbI$_3$ has been shown to improve the optical properties of the layers [39]. The beneficial effect of K$^+$ was demonstrated by Stranks et al.[40] who employed KI additive for triple cation double halide PVK synthesis. Potassium halides have been shown to passivate defects at the grain boundaries and PVK layers near interfaces [40,41].

To the best of our knowledge, the use of NH$_4$Cl and KCl co-additives for the synthesis of Cs$_x$FA$_{1-x}$PbI$_3$ layers has never been reported. In the present work, we show that KCl favors the obtaining of a pure perovskite α-phase without PbI$_2$ impurity and blocks the iodide mobility. Mixing both NH$_4$Cl and KCl leads to a synergistic effect since the prepared layers have large grains, no pinholes, and low PbI$_2$ impurity level. It results in solar cells with high efficiency and negligible hysteresis. Moreover, by using glow-discharge optical emission spectroscopy (GD-OES) we have been able to show that KCl additive blocks iodide migration. We have conspicuously correlated the absence of hysteresis and the absence of I movement inside the PVK under the application of an electric field. Overall, this strategy has led to a stabilized efficiency close to 20.1%, a performance among the best for Cs$_x$FA$_{1-x}$PbI$_3$ solar cells. Furthermore, the optimized device presented an excellent stability.

2. Results and Discussion

$Cs_xFA_{1-x}PbI_3$ appears as one of the most interesting methylammonium-free perovskite compounds for photovoltaic application since it presents an optical bandgap close to the optimum, excellent opto-electronic properties and a good thermal stability. This work aimed at preparing the best $Cs_xFA_{1-x}PbI_3$ layers applied as the absorber in solar cells with the structure presented in **Figure 1a**. The first step was to investigate the effect of *x* on the solar cell performances (**Section A**, Supporting Information). By varying *x* up to 0.2, we found that the best PCE was reached for *x*=0.1 (**Table S1** Supporting Information). This composition was then retained in the rest of our study. The cells prepared from stochiometric solution of CsI, FAI and PbI_2 precursors achieved a maximum efficiency of only 16.13% and a stabilized PCE of 15.73%. The open-circuit voltage (V_{oc}) and fill factor (*FF*) parameters were low. The short-circuit current density (J_{sc}) was 23.8 mA.cm^{-2}, in good agreement with the external quantum efficiency (EQE) curve integration which gave 23.4 mA.cm^{-2} (**Figure 1c**). These cells also exhibited a large hysteresis with a hysteresis index (HI) measured at 28% (**Table 1**). These results were confirmed by the statistical analysis in **Figure 1d**. To boost the performances and suppress the hysteresis we developed the use of chloride additives in the PPS.

Table 1 Best cells *J-V* curves parameters of $Cs_{0.1}FA_{0.9}PbI_3$ solar cells prepared without and with different optimized chloride additives.

Name	Scan direction	V_{oc} [V]	J_{sc} [mA cm^{-2}]	*FF* [%]	PCE [%]	HI[%][a]
w/o	Reverse	0.941	23.82	71.92	16.13	28
	Forward	0.837	23.88	58.24	11.65	
KCl	Reverse	0.992	25.24	76.54	19.16	1
	Forward	0.993	25.17	75.99	18.99	
KCl/NH$_4$Cl	Reverse	1.012	25.21	78.61	20.05	3
	Forward	1.013	24.94	76.73	19.39	

[a]HI=(PCE$_{Rev}$-PCE$_{For}$)*100/PCE$_{Rev}$
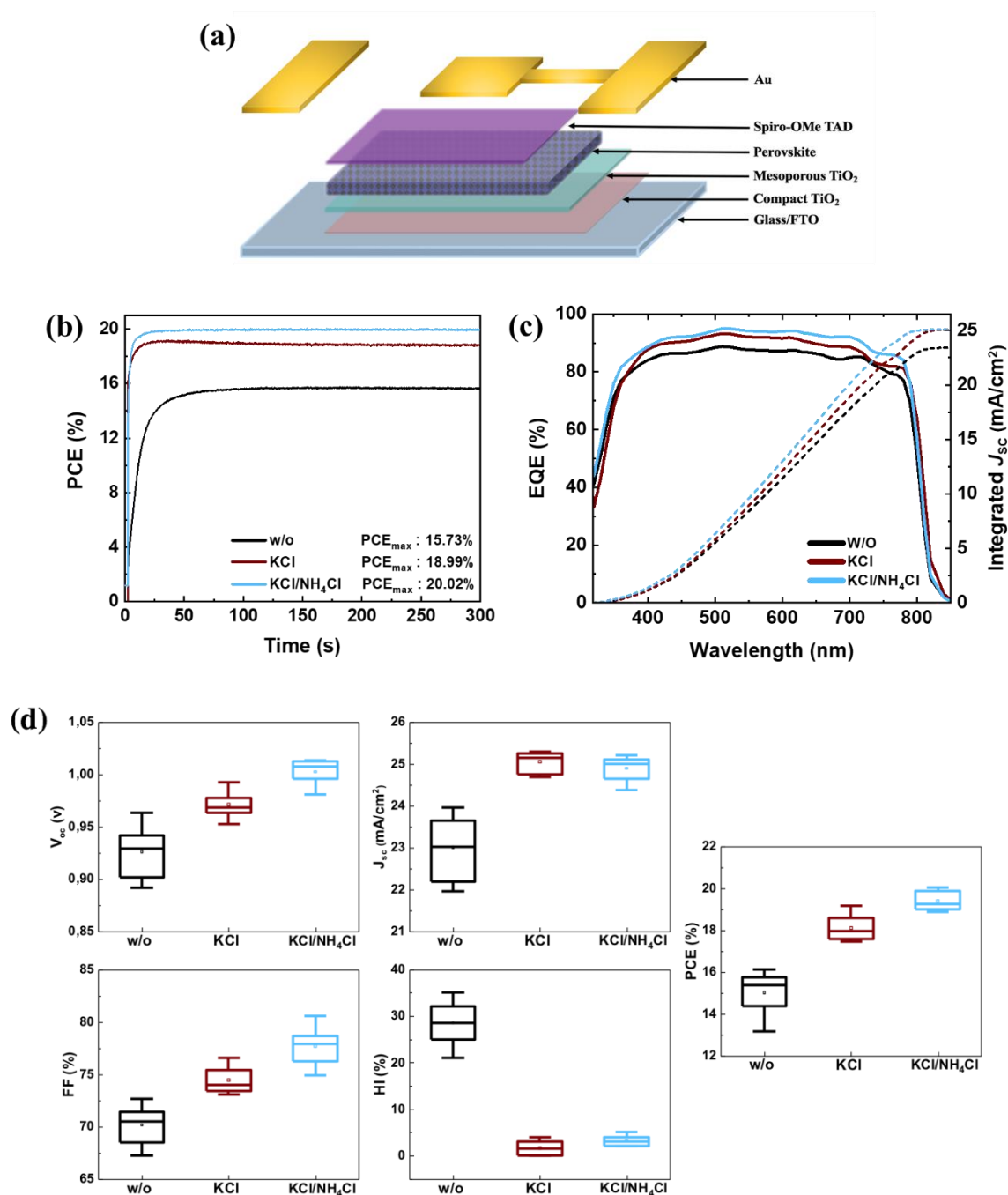
Figure 1. (a) Exploded schematic view of the PSC structure. (b) Maximum power point (MPP) tracking and best stabilized efficiency. (c) EQE curves and integrated J_{sc} curves of the best PSCs. (d) Statistical analysis of the optimized PSCs *J-V* curve parameters and PCE.

A few works have reported the beneficial effects of potassium chloride (KCl) on the properties and performances of various methylammonium-containing perovskites such as MAPbI$_3$ [35] and

$(Cs,FA,MA)Pb(I,Br)_3$ [37]. However, to the best of our knowledge, it has never been employed for assisting the synthesis of methylammonium-free perovskite layers. KCl additive cannot be used in large amount because K^+ is not eliminated upon annealing at 150°C and it remains in the layer. Moreover, the solubility of potassium chloride in the PPS is quite limited. Consequently, we investigated PPSs with KCl at 0 mol%, 5 mol%, 9 mol% and 13 mol% of the molar PbI_2 content (**Section B,** Supporting Information). The scanning electron microscopy (SEM) images of the resulting layers are shown in **Figure S2** (Supporting Information). KCl additive prevents the formation of pinholes and of bright grains that are assigned to PbI_2. XRD measurements (**Figure S3**, Supporting Information) show that this additive does not improve the crystallinity, but the obtained compounds are α-$Cs_{0.1}FA_{0.9}PbI_3$ pure phase. The absence of PbI_2 is assigned to a better solubilization of PbI_2 with formation of iodoplombate complexes in DMF/DMSO solvent mixture in the presence of KCl. We have also noted that increasing the KCl additive concentration leads to a slight decrease in the (001) and (002) PVK peak position and then to an increase of the lattice parameters (**Figure S3b**, Supporting Information). It shows that K^+ enters in the crystal lattice. Since the ionic radius of K^+ is smaller than the FA^+ one, the former would be present as interstitial. **Figure S4** (Supporting Information) reveals the best measured absorbance for 9 mol%. The statistical analysis of the performances of PSCs prepared with various amounts of KCl is disclosed in **Figure S5** (Supporting Information). The maximum PCE was achieved for 9 mol% KCl at 19.16% which is a marked improvement compared to 16.13% for the control. A very interesting observation is that, compared to the pristine cell (w/o), employing KCl additive suppressed the *J-V* curves hysteresis (**Figure S11a**, Supporting Information). In the rest of this work, the 9 mol% KCl layers and solar cells have been retained as benchmarks for KCl additive (noted KCl).

We have also shown separately that NH_4Cl additive is also beneficial for the $Cs_{0.1}FA_{0.9}PbI_3$ layer crystallinity, grain size and PSC performances (see **Section C**, Supporting Information). We then mixed the two chloride additives to obtain a synergistic beneficial effect for the performances and properties of the PSCs. Various mixtures were investigated (see **Section D**, Supporting Information) and the best performance was found for KCl at 5 mol% and NH_4Cl at 30 mol%. The PCE attained a remarkable 20.05% value. Adding an optimized amount of KCl or KCl/NH_4Cl, mixture led to a significant

6

improvement of J_{sc} (**Table 1**). External quantum efficiency (EQE) spectra in **Figure 1c** conspicuously show the beneficial effect of chloride additives on EQE over the whole visible wavelength. From the integration of these curves, we calculated J_{sc} of 23.42 mA.cm^{-2}, 25.08 mA.cm^{-2} and 25.11 mA.cm^{-2} for the w/o, KCl and KCl/NH$_4$Cl solar cells, respectively. These values are in good agreement with those measured on *J-V* curves (**Table 1**). The other *J-V* curves parameters, V_{oc} and *FF*, were also ameliorated by co-additives and the hysteresis suppression was maintained (**Figure S11a,b**, Supporting Information). These conclusions, made for the best cells, were confirmed by the statistical analysis disclosed in **Figure 1d**.
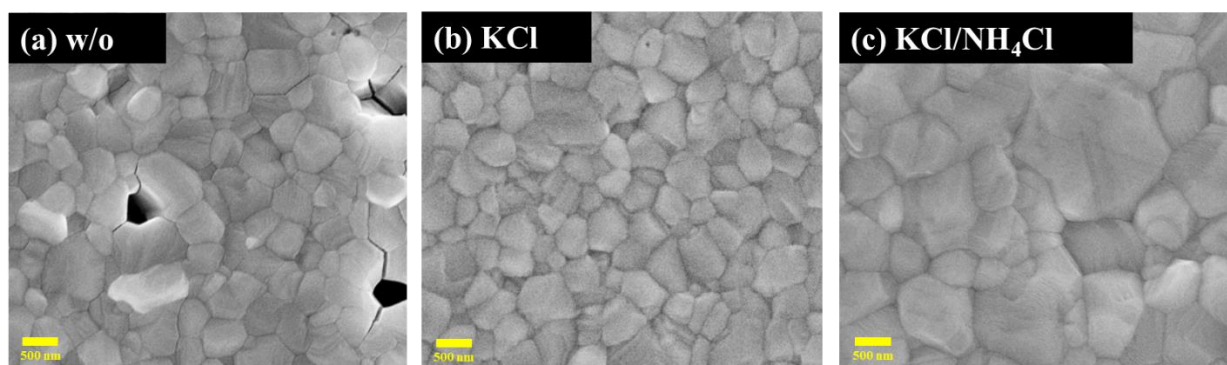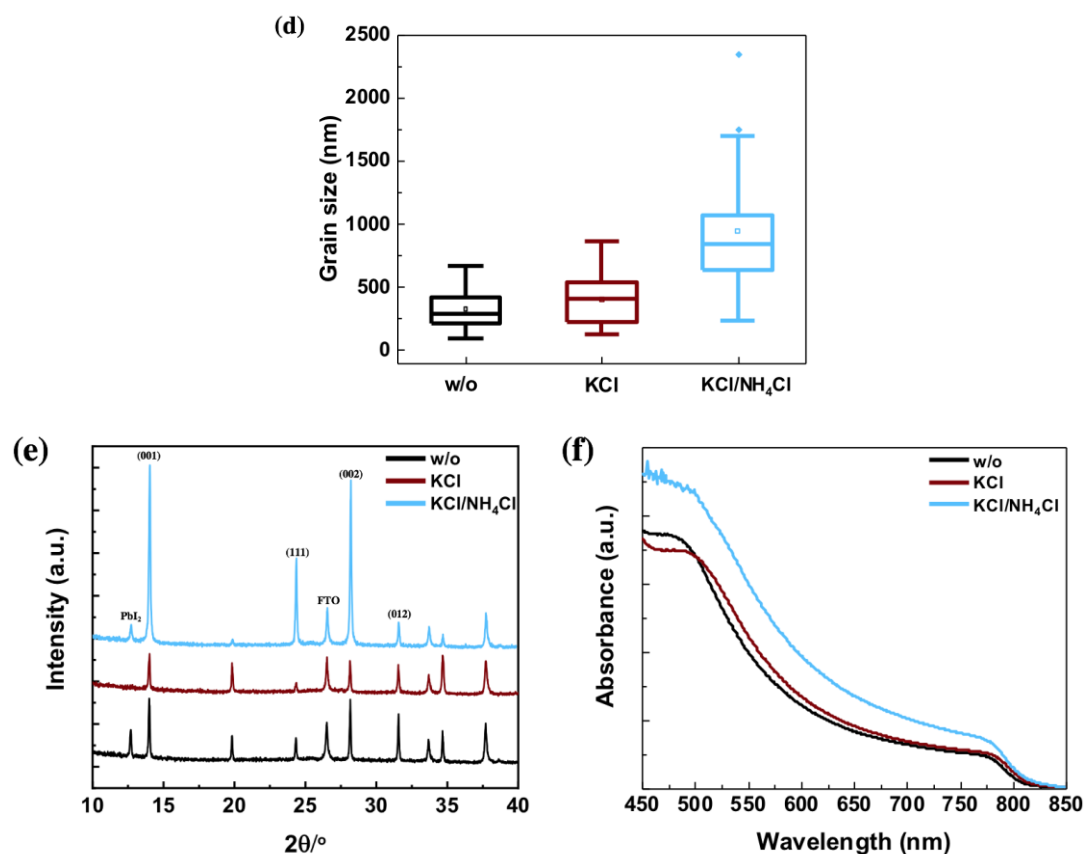
Figure 2. (a-c) SEM top views (scale bar 500 nm), (d) grain size distribution, (e) XRD patterns and (f) absorbance of w/o, KCl and KCl/NH$_4$Cl Cs$_{0.1}$FA$_{0.9}$PbI$_3$ layers.

The steady-state performances of the various cells were measured by tracking the maximum power point (MPP) (**Figure 1c**). The normalized curves (**Figure S11c**, Supporting Information) clearly indicate that the w/o PSC presented a slow time response compared to the two others. They reached their PCE plateau after about 100s. The slow response of these cells is in line with their large hysteresis. On the other hand, for devices prepared with KCl, the steady state was reached much more rapidly, that is after about 20s. It confirms the beneficial effect of K$^+$ on the device time response. The 15.73% stabilized PCEs of the w/o cell must be compared to the 16.13% one measured on the reverse scan. In the presence of KCl, the discrepancy between these two values was very low and we found a remarkable 20.02% stabilized PCE for the KCl/NH$_4$Cl cell, which is very close to the 20.05% measured on the *J-V* curves reverse scan.

Advanced characterizations helped us to better understand the effects of co-additives on the solar cell performances and electrical response. The SEM top-views (**Figure 2a-c**) showed that the KCl additive eliminated the pinholes and that, adding NH_4Cl in the mixture led to the formation of large grains. The mean grain size was very large at 937 nm and much larger than for the w/o (327 nm) and KCl (392 nm) samples (**Figure 2d**). SEM cross-sectional views (**Figure S12a-c**, Supporting Information) indicate that the *mp*-TiO_2/PVK interface was greatly improved by the additives which suppressed the presence of voids. They also promoted the formation of large grains and produced a monolithic structure which is the best one for a fast charge carriers' transfer to the interfaces.[18] On XRD patterns in **Figure 2e**, the presence of PbI_2 was suppressed by KCl whereas this phase was dramatically reduced in the KCl/NH_4Cl layer which was mainly made of α-phase $Cs_{0.1}FA_{0.9}PbI_3$. Moreover, XRD peaks were more intense for the mixture due to a better crystallinity. The KCl/NH_4Cl pattern was dominated by the (001) and (002) peaks showing a texturation of the layer. **Figure 2f** compares the absorbance spectra of the optimized samples. The use of chloride additive increased light absorption between 500 nm and 800 nm. The mixed additives lead to a stronger absorbance which can be linked to a better control of the film growth that gives rise to thicker layers (measured on the cross-section views at 280 nm, 310 nm and 330 nm for w/o, KCl and KCl/NH_4Cl samples, respectively (**Figure S12**, Supporting Information)). The absorption band-edge was similar for the four samples. The Tauc plots of the absorbance spectra in **Figure S12d** (Supporting Information) provide an optical bandgap of ~1.545 eV for the various PVKs, either with or without chloride additives. This value is closer to the optimum one for PV application compared to $MAPbI_3$ or triple cation perovskites.[44] Larger PVK grains, better crystallinity and film absorbance for the KCl/NH_4Cl layers are at the origin of the better J_{sc}, V_{oc} and *FF* compared to the control. The perovskite layers composition was investigated by Energy-dispersive X-ray spectroscopy (EDX) mapping. **Figure S13a-d** (Supporting Information) shows that I and Cs were detected in all samples. On the other hand, Cl, present in a large amount in the KCl and KCl/NH_4Cl PPSs, was not detected by EDX in the final films. It confirms our observation made for $FA_{1-x}MA_xPbI_3$ perovskite layers prepared in the presence of MACl additive that this element is mostly eliminated upon the annealing step above 150°C

[18,19]. K element was detected in the samples prepared with KCl additive and appeared quite homogeneously distributed.
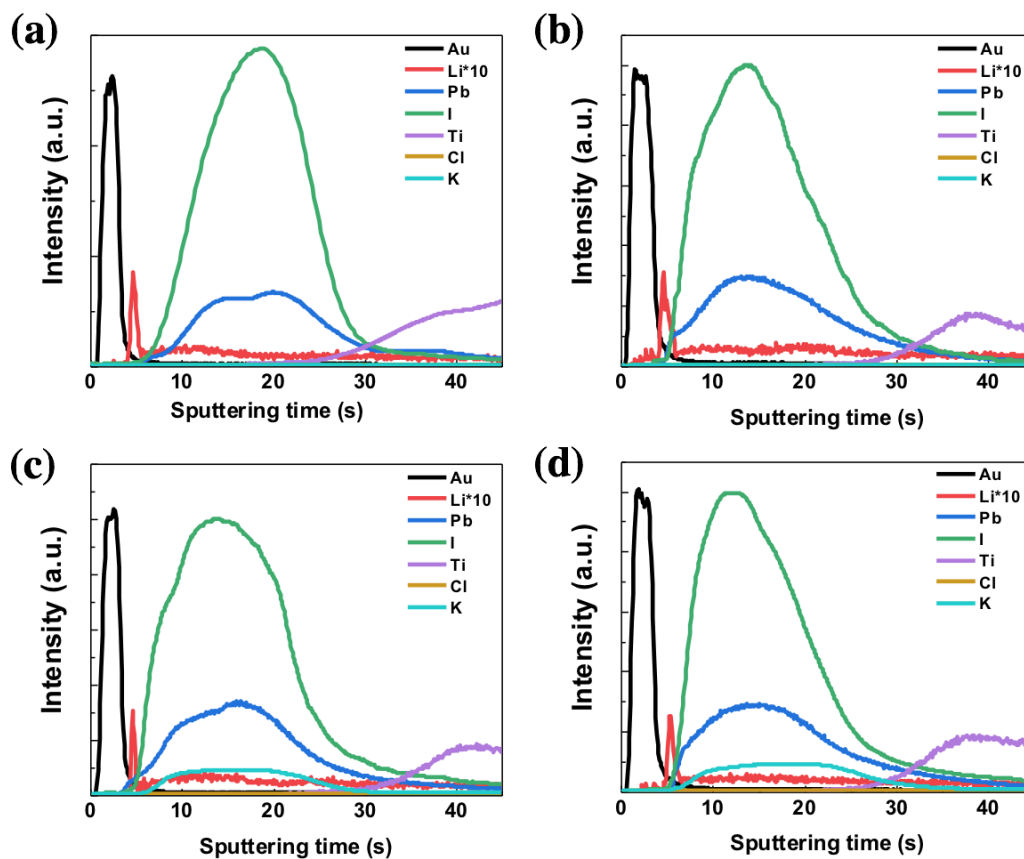

Figure 3. Element distribution across the entire devices measured by GD-OES for non-polarized solar cells: (a) w/o-cell, (b) NH_4Cl-cell, (c) KCl-cell and (d) KCl/NH_4Cl-cell.

To better understand the positive effect of K^+, present in the perovskite layers, on the PSC electrical response, we conducted Glow-Discharge Optical Emission Spectrometry (GD-OES) experiments on the full devices. Up to now, in the few papers where this technique was employed, only $MAPbI_{1-x}Cl_x$-based half-cell [49] or full cells [50-52] were investigated. Our experiments consisted in directly Ar-sputtering the full devices and to detect the optical emission of the elements etched-released from the various layers. It allowed us to get a depth-profile distribution of the devices' constituent elements. In a first step we measured the compositional profile of the full cells and investigated the effect of $Cs_{0.1}FA_{0.9}PbI_3$ growth conditions on these profiles. GD-OES allowed us to conspicuously distinguish the various layers composing the solar cells. We followed the main inorganic elements of the structure, namely Au, Li,

Pb, I, Ti, Cl and K while our GD-OES system did not enable us to accurately follow N, O, C and H elements. In **Figure 3**, they appeared successively at increasing Ar sputtering time. One can note that the relative intensity of the various elements does not correspond directly to the relative concentrations due to the independent sputtering and emission yields for each element. First, Au of the back-electrode appeared. Then we observed a sharp Li peak corresponding to the dopant in the Spiro-OMeTAD organic hole transporting layer. This organic layer was etched rapidly. The signal of Li, present in small quantity, is multiplied by 10 in **Figure 3**. Then the perovskite layer appeared after 7s of sputtering time with the presence of both Pb and I. We remark that, for the NH_4Cl, KCl and KCl/NH_4Cl samples, the I and Pb signals extent over a longer time, with the presence of a tail. It can be explained by the fact that these films were thicker than the w/o one. After 28s-30s, Ti of TiO_2 appeared. We have noted that no Cl could be detected in the perovskite layer (**Figure S13e**, Supporting Information), confirming our EDX analysis. GD-OES is a highly sensitive technique, therefore, if Cl is present, its amount is less than 0.1 at.%. This element was also not detected by XPS technique (not shown). Most of it is eliminated upon annealing. On the other hand, we could clearly detect the presence of K in the KCl and KCl/NH_4Cl samples. This element was homogeneously distributed over the entire perovskite layer thickness. No depletion on its top was observed, confirming that K was not, even partly, eliminated upon the annealing process.
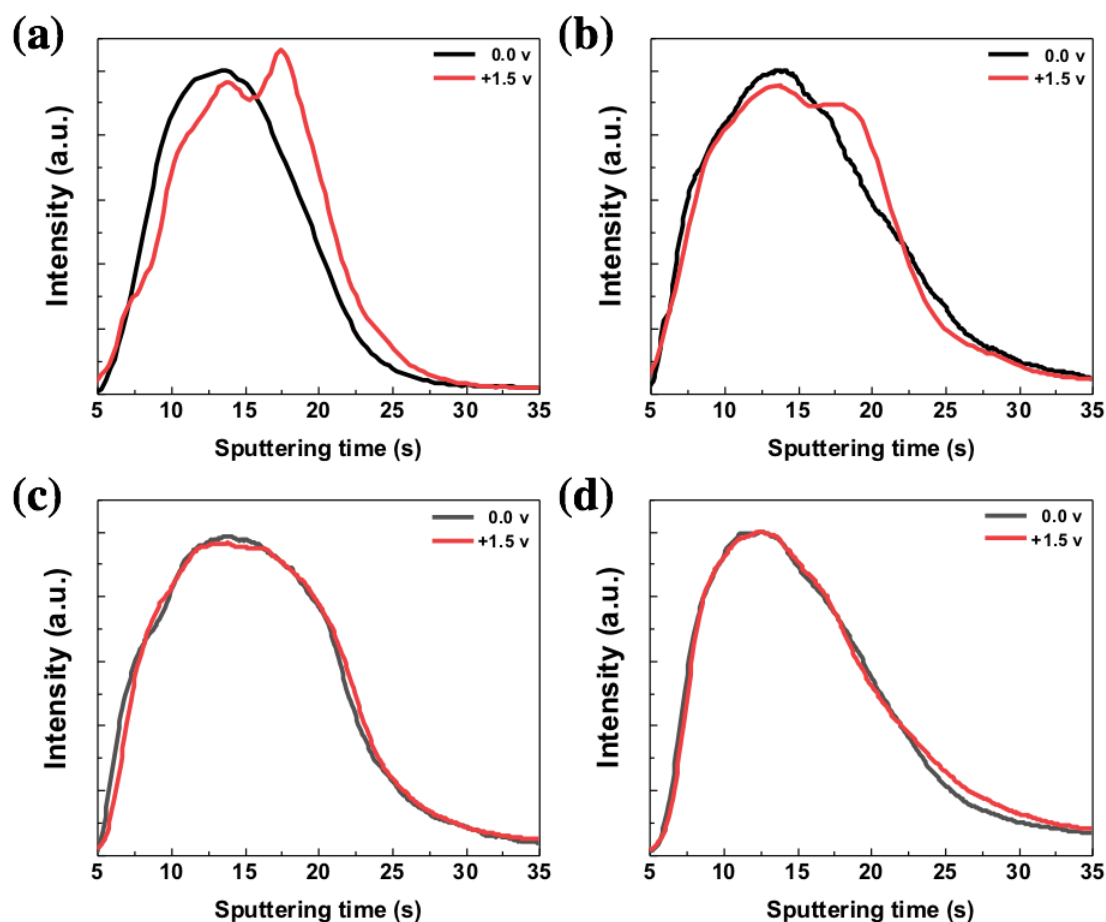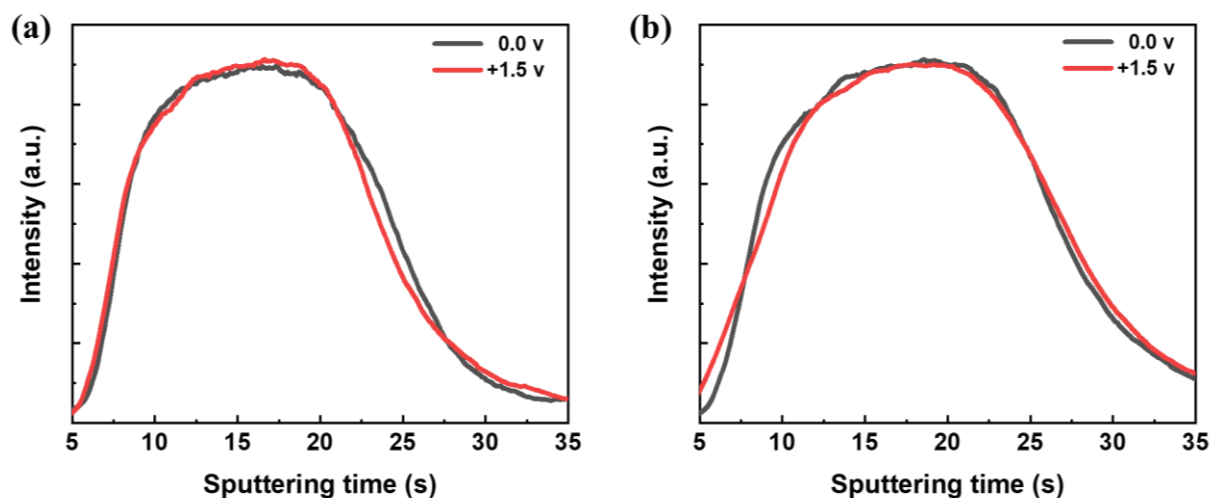
Figure 4. GD-OES profile of iodine in the perovskite films after polarization at 0V (black traces) and after polarization at 1.5 V (red traces). (a) w/o, (b) NH_4Cl, (c) KCl and (d) KCl/NH_4Cl.

Our objective was then to directly observe the effect of K doping on the mobility of iodide. To this end, we conducted GD-OES measurements on full devices after their polarization at a certain voltage. In **Figure 4**, we compare the I element profile for cells polarized at 0V and cells polarized at 1.5V for 30s. A profile change was clearly seen for the sample prepared without additive (**Figure 4a**). The initial peak (black trace) was split after applying an electric field (red trace). Two I element fractions could then be distinguished: a fixed one and a mobile one which moved toward the positively polarized TiO_2 electrode. The technique visualizes that large iodide movement occurred in the layer [51]. In the case of the NH_4Cl cell (**Figure 4b**), the same phenomenon occurred but in a less extend. NH_4Cl samples were better crystallized than the w/o ones, they contained less defects. Therefore, the fraction of mobile species was reduced. On the other hand, for the two cells prepared using KCl additive, namely KCl and

KCl/NH$_4$Cl, the iodine profiles, measured without (black trace) and with (red trace) application of an electric field, overlapped. It shows that potassium has the remarkable property of blocking the ionic mobility. As ionic migration in halide perovskites is considered to occur through native point defects such as vacancies [53-55] and/or interstitials [55] we can conclude that K passivates these defects present in the structure. Stranks et al.,[40] who worked on the triple-cation (Cs,FA,MA)Pb(I$_{0.85}$Br$_{0.15}$)$_3$ perovskite prepared in the presence of KI, found passivating potassium halide layers formed at the layer interfaces and at the grain boundaries, these parts being the most defect-rich. Our characterizations have not allowed us to precisely localize the passivated defects' location, but it seems reasonable to say that the mobile I component must be more present at the grain periphery and grain boundaries. The K$^+$ action likely occurs through its ability to combine with mobile iodide. It is noteworthy that our GD-OES measurements perfectly correlate with the hysteresis phenomenon quantified on the *J-V* curves (**Table 1**, **Figure 1d**). For the w/o sample, with the largest hysteresis (HI~28%), the iodide displacement is large. For the NH$_4$Cl sample, with intermediate hysteresis (HI~18%), the displacement is present but not so important. Finally, for the KCl cell and KCl/NH$_4$Cl cell, iodide is blocked while these cells are almost hysteresis-free (HI~1%-3%). It proves that hysteresis is due to the mobility of iodide in the layer. Blocking this mobility leads to hysteresis-free PSCs. We can note that this work is the first which correlates the iodide blocking, directly observed by GD-OES, and the absence of hysteresis. **Figure 5** shows the K element profile without and with application of an electric field. This profile was unchanged for both KCl and KCl/NH$_4$Cl cells. We can conclude that the passivation is perfectly stable, and that potassium is at the origin of a robust passivation of defects.

Figure 5. GD-OES profile of K element in the perovskite films after polarization at 0V (black lines) and after polarization at 1.5 V (red lines). (a) KCl and (b) KCl/NH$_4$Cl.

The future of the PSC technology will mainly depend on the ability to obtain highly stable devices. Our interest in Cs$_x$FA$_{1-x}$PbI$_3$ compounds was motivated by eliminating MA, this component being a source of instability. In **Figure 6a**, the three unencapsulated and optimized Cs$_{0.1}$FA$_{0.9}$PbI$_3$ cells have been continuously tracked under the solar simulator delivering 1 sun at ambient relative humidity (50-60%). Their evolutions are compared to other PSCs: FAPbI$_3$ and two MA containing perovskites, namely MAPbI$_3$ and Cs$_{0.08}$FA$_{0.80}$MA$_{0.12}$Pb(I$_{0.88}$Br$_{0.12}$)$_3$ (noted CsFAMA) which have been studied in detail in our previous work [44]. We first confirm that α-FAPbI$_3$ is highly unstable since it is rapidly transformed into the photoinactive δ-FAPbI$_3$. Secondly, we observed a poor stability of MAPI and KCl cells with a PCE loss of 29% after 180 min. It means that the passivation of native defect sites by K$^+$ and then the blocking iodide mobility is insufficient to stabilize the halide perovskite under these conditions. The CsFAMA cell was also not very stable. The stability of Cs$_{0.1}$FA$_{0.9}$PbI$_3$ increased in the order: w/o and KCl/NH$_4$Cl. Mixing the two chloride additives is then a successful strategy to get high stability since the KCl/NH$_4$Cl devices retained 97% of their initial PCE after 180 min.
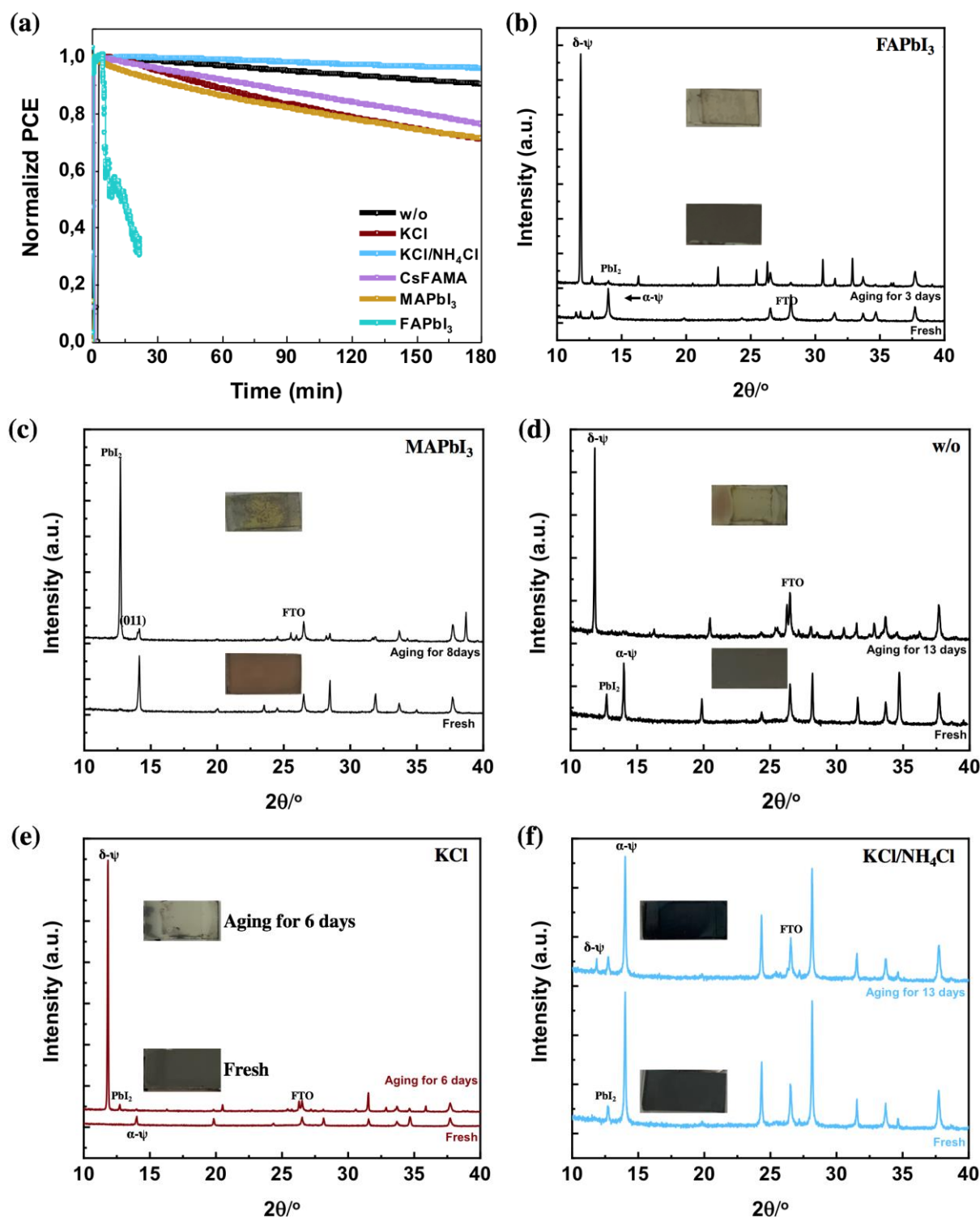
Figure 6. (a) MPP Tracking of $Cs_{0.1}FA_{0.9}PbI_3$ cells prepared without and with chloride additives, FAPbI₃, MAPbI₃ and CsFAMA cells. Normalized power outputs under continuous one sun AM1.5 G illumination (unencapsulated devices, relative humidity (RH) ~50%). (b-g) XRD patterns of perovskite samples: fresh and after aging under ambient air conditions (T°=20-25°C, RH=50-60%) (b) FAPbI₃ (aged 3 days), (c) MAPbI₃ (aged 8 days), (d-g) $Cs_{0.1}FA_{0.9}PbI_3$: (d) w/o (aged 13 days), (e) NH₄Cl (aged 13 days), (f) KCl (aged 6 days) and (g) KCl/NH₄Cl (aged 13 days). Insets are layer pictures before and after aging.

We also tested the resistance of the various perovskites to humidity and other ambient degrading agents by following their XRD pattern and aspect after storage under the ambient atmosphere (**Figure 6**). **Figure 6b** confirms that α-FAPbI$_3$ is highly unstable. The (001) plane of the black α-phase disappeared after only 3 days of aging. It was transformed into the more stable yellow δ-phase which is photo-inactive. The change is conspicuously visualized by the sample color. MAPbI$_3$ is also poorly stable (**Figure 6c**). Its main (011) diffraction peak at 14.1° almost fully disappeared after 8 days of aging. It was replaced by a strong (001) PbI$_2$ peak at 12.7°. In this case the perovskite decomposes, MA is outgassed and a yellow PbI$_2$ layer is formed as shown in the inserted picture. **Figure 6d** shows that the w/o sample was fully degraded after 13 days of aging and was also poorly stable. The (001) α-phase and (001) PbI$_2$ peaks at 14.0° and 12.7°, respectively, disappeared while a strong δ-phase peak at 11.8° dominated the pattern. The sample color changed from dark black to yellow. It demonstrates that eliminating MA is not sufficient to stabilize the hybrid perovskite. In the case of the KCl sample (**Figure 6e**), PbI$_2$ was not present in the fresh sample. After only 6 days, the sample was fully degraded. The main degradation phase was the perovskite δ-phase but some PbI$_2$ phase was also formed. Adding NH$_4$Cl clearly stabilizes the Cs$_{0.1}$FA$_{0.9}$PbI$_3$ sample (**Figure S14**, Supporting Information) since after 13 days the α-phase was still present. The stabilization is assigned to the beneficial effect of NH$_4$Cl which allows the growth of larger grains. However, the remarkable result is the synergetic effect of NH$_4$Cl and KCl on the layer stability. Indeed, in **Figure 6g**, the layers, non-protected by overlayers and encapsulation and then directly exposed to the degradation agents (moisture, UV, oxygen…) were still dark black after 13 days. The small PbI$_2$ peak at 12.7° did not evolve and only a small perovskite δ-phase peak was present.

Finally, the thermal stability was tested by heating the layers 4 hours at 130°C in N$_2$ atmosphere. **Figure S15** (Supporting Information) compares the XRD patterns of FAPbI$_3$, MAPbI$_3$ and Cs$_{0.1}$FA$_{0.9}$PbI$_3$ samples before and after this treatment. In all cases, a peak at 12.7° appeared or grew due to the release of the organic components and formation of PbI$_2$. The fastest degradation was found for

MAPI which contains MA. For the other compounds, the perovskite phase remained the main one and we clearly observed that the KCl/NH$_4$Cl sample was the less degraded of the series.

3. Conclusions

In summary, we developed the use of two new chloride additives, ammonium chloride and potassium chloride, for the preparation of layers of methylammonium-free and bromide-free Cs$_{0.1}$FA$_{0.9}$PbI$_3$ perovskite. We have shown that KCl plays a favorable role on phase purity and that potassium, integrated homogeneously in the layer, passivates defects in the structure. By using this additive, hysteresis-free devices have been fabricated. Moreover, we have been able to demonstrate, by direct observation, that the hysteresis suppression is due to the ability of K$^+$ to block iodide species migration in the PVK layer. K is insensitive to the electric field and robustly passivates native defect sites. However, blocking the ionic mobility is insufficient to fully stabilize the devices. Further optimizations have been done, notably to control the crystallization of the PVK, by using NH$_4$Cl as a co-additive. They have permitted to get highly stable layers and devices. By this approach, we prepared methylammonium-free, hysteresis-free PSCs with a stabilized PCE achieving 20.02%.

4. Experimental Section

4.1 Preparation of substrate, compact-TiO$_2$ and mesoporous TiO$_2$ Layers

Fluorine-doped SnO$_2$ (FTO) substrates (TEC 7 from Pilkington) were etched pattern by zinc powder and 10% HCl solution prior to be cleaned with soap and water. The substrates were subsequently immersed for 20 min in a concentrated 2.2 M NaOH in ethanol/water (10:1 v/v %) and then rinsed with deionized water in an ultrasonic bath for 15 min [56]. The substrates were subsequently heated at 500°C for 15 min. The compact TiO$_2$ hole blocking layer, noted *c*-TiO$_2$, was prepared by aerosol spray pyrolysis. The TiO$_2$ nanoparticle solution employed for the preparation of the mesoporous layer, noted *mp*-TiO$_2$, was prepared in advance and stirred for at least 12h. The TiO$_2$ NR30-D paste (from Greatcell)

was diluted in ethanol with a 1:7 w/w ratio. 45 μL of the solution was dropped on the compact TiO_2 layer and spin-coated at 2000 rpm for 15 s. The layer was then dried on a hotplate at 70 °C for 5-10 min and finally heated at 500 °C under an air flux for 30 min, cooled down to 200 °C and removed from the hotplate.

4.2 Preparation of the perovskite layers:

[$Cs_{0.1}FA_{0.9}PbI_3$] A mixed cation PPS with a 1.0M concentration was prepared by mixing 156 mg Formamidinium iodide (FAI, greatcell), 461 mg of Lead iodide (PbI_2 , TCI), and 26 mg (x=0.10), Cesium Iodide (CsI, TCI) in 900 μL DMF and 100 μL DMSO. The solutions were stirred for a minimum of 2 h at 50 °C in a N_2 glovebox. 45 μL of this solution was placed on top of the substrates. A two-step spin-coating program was employed: first spinning at 1000 rpm for 10 s and then at 4000 rpm for 20 s. 100 μL of chlorobenzene was dripped 15~20 s after the starting of the spinning routine. The films were then annealed at 155 °C for 20 min.

[$Cs_{0.1}FA_{0.9}PbI_3$ with Potassium Chloride] A mixed cation PPS with a 1.0M concentration was prepared by mixing 156 mg of formamidinium iodide (FAI, greatcell), 461 mg of PbI_2 (TCI), 26 mg Cesium Iodide (CsI, TCI) and 3.7 mg, 6.7 mg, 9.7 mg (5 mol%, 9mol%, 13 mol%, respectively) of Potassium Chloride (KCl, Alfa aesar) in 900 μL DMF and 100 μL DMSO. The solutions were stirred for a minimum of 3-4 h at 50 °C in a N_2 glovebox. The spin-coating process was the same as before. These films and corresponding solar cells are noted KC-5, KC-9 and KC-13.

[$Cs_{0.1}FA_{0.9}PbI_3$ with Potassium Chloride and Ammonium Chloride] A mixed cation PPS with a 1.0M concentration was prepared by mixing 156 mg of Formamidinium iodide (FAI, greatcell), 461 mg of Lead iodide (PbI_2, TCI), 26 mg Cesium Iodide (CsI, TCI), 10 mg and 15 mg (20 mol% and 30 mol%) of Ammonium Chloride (NH_4Cl, Alfa aesar) and 3.7 mg and 6.7 mg (5 mol% and 9 mol%) of Potassium Chloride (KCl, Alfa aesar) in 900 μL DMF and 100 μL DMSO. The solutions were stirred for a minimum of 7-8h at 50 °C in a N_2 glovebox. The spin-coating process was the same as before. These films and corresponding solar cells are noted KC-5/AC-20, KC-5/AC-30 (also noted KCl), KC-9/AC-20 and KC-9/AC-30.

The hole transporting Information (HTM) solution was prepared by dissolving 78 mg of Spiro-OMeTAD (Borun New Material Technology) in 1 mL of chlorobenzene. Then, 17.9 µL of bis(trifluoromethylsulfonyl)imide lithium salt solution (Li-TFSI) (Sigma Aldrich) solution (517 mg in 1 mL ACN), 30.4 µL of TBP (tert-butylpyridine) (Sigma Aldrich) and 14 µL of tris(2-1H-pyrazol-1-yl)-4-tert-butylpyridine)-cobalt(III) tris (bis(trifluoromethylsulfonyl)imide) (Dyesol, FK209) (376 mg in 1 mL acetonitrile) were added to this solution. 40 µL of the HTM solution was spin-coated at 4000 rpm for 30 s [57]. Finally, the device was completed by thermally evaporating a 70-80 nm thick gold back contact on the Spiro-OMeTAD layer.

4.3 Layers and devices characterizations

The structure of the organometal lead perovskite films was characterized by a PANanalytical X-Pert high-resolution X-ray diffractometer (XRD) operated at 40 kV and 45 mA and using the CuKα radiation with λ= 1.5406 Å. The film specular absorbance was measured by a Cary 5000 UV-Vis-NIR spectrophotometer. A glass/FTO/*c*-TiO$_2$/*mp*-TiO$_2$ sample was employed for the baseline. The morphology of perovskite thin films was measured using a field-emission SEM equipment (Zeiss Supra 40) in the in-lens mode. The EDX mapping spectra were measured with a Quantax system from Compact 30mm Brucker operated at 15 kV. Glow-Discharge Optical Emission Spectrometry (GD-OES) analyses were performed using a HORIBA Jobin Yvon GD Profiler 2 equipment. This instrument was equipped with a RF-generator (at 13.56 MHz), a standard HORIBA Jobin Yvon glow discharge source with a cylindrical anode of 4 mm internal diameter and two optical spectrometers (a polychromator and a monochromator) for fast-optical detection. The Ar plasma was generated at an Ar pressure of 420 Pa and an applied power of 17 W. The solar cell was mounted on an O-ring at one side of the plasma chamber and used as a cathode.

The solar cells *J-V* curves were recorded by a Keithley 2410 digital sourcemeter, using a 0.1 V.s^{-1} voltage scan rate. The solar cells were illuminated with a solar simulator (Abet Technology Sun 2000) filtered to mimic AM 1.5G conditions (100 mW cm^{-2}). The illuminated surface was delimited by a black mask with an aperture diameter of 3 mm. The power density was calibrated at 100 mW cm^{-2} by the use of a reference silicon solar cell.

Supporting Information ((delete if not applicable))
Supporting Information is available from the Wiley Online Library or from the author.

Acknowledgements

References

[1] H. S. Kim, C. R. Lee, J. H. Im, K. B. Lee, T. Moehl, A. Marchioro, S. J. Moon, R. Humphry-Baker, J. H. Yum, J. E. Moser, M. Grätzel, N. G. Park, *Sci. Rep.* **2012**, *2*, 591.

[2] M. M. Lee, J. Teuscher, T. Miyasaka, T. N. Murakami, H. J. Snaith, *Science* **2012**, *338*, 643–647.

[3] M. Liu, M. B. Johnston, H. J. Snaith, *Nature* **2013**, *501*, 395–398.

[4] J. Burschka, N. Pellet, S. J. Moon, R. Humphry-Baker, P. Gao, M. K. Nazeeruddin, M. Grätzel, *Nature* **2013**, *499*, 316–319.

[5] J. Zhang, P. Barboux, T. Pauporté, *Adv. Energy Mater.* **2014**, *4*, 1400932.

[6] J. Zhang, E. J. Juárez-Pérez, I. Mora-Seró, B. Viana, T. Pauporté, *J. Mater. Chem. A.* **2015**, *3*, 4909–4915.

[7] P. Wang, Z. Shao, M. Ulfa, T. Pauporté, *J. Phys. Chem. C* **2017**, *121*, 9131–9141.

[8] P. Wang, M. Ulfa, T. Pauporté, *J. Phys. Chem. C* **2018**, *122*, 1973−1981.

[9] S. H. Turren-Cruz, A. Hagfeldt, M. Saliba, *Science* **2018**, *362*, 449-453.

[10] N. J. Jeon, H. Na, E. H. Jung, T. Y. Yang, Y. G. Lee, G. Kim, H. W. Shin, S. I. Seok, J. Lee, J. Seo, *Nature Energy* **2018**, *3*, 682–689.

[11] Q. Jiang, Y. Zhao, X. W. Zhang, X. L. Yang, Y. Chen, Z. M. Chu, Q. F. Ye, X. X. Li, Z. G. Yin, J. B. You, *Nature Photonics* **2019**, *13*, 460–466.

[12] E. H. Jung, N. J. Jeon, E. Y. Park, C. S. Moon, T. J. Shin, T. Y. Yang, J. H. Noh, J. Seo, *Nature* **2019**, *567*, 511–515.

[13] NREL PV Research Cell Record Efficiency Chart, https://www.nrel.gov/pv/cell-efficiency.html (accessed: November 2020).

[14] A. Mei, X. Li, L. Liu, Z. Ku, T. Liu, Y. Rong, M. Xu, M. Hu, J. Chen, Y. Yang, M. Grätzel, H. Han, *Science* **2014**, *345*, 295-298.

[15] G. Grancini, C. Roldan-Carmona, I. Zimmermann, E. Mosconi, X. Lee, D. Martineau, S. Narbey, F. Oswald, F. De Angelis, M. Graetzel, M. K. Nazeeruddin, *Nature Commun.* **2017**, *8*, 15684.

[16] M. Xu, W. Ji, Y. Sheng, Y. Wu, H. Cheng, J. Meng, Z. Yan, J. Xu, A. Mei, Y. Hu, Y. Rong, H. Han, *Nano Energy* **2020**, *74*, 104842.

[17] M. Ulfa, P. Wang, J. Zhang, J. Liu, W. Daney de Marcillac, L. Coolen, S. Peralta, T. Pauporté, *ACS Appl. Mater. Interfaces* **2018**, *10*, 35118–35128.

[18] T. Zhu, D. Zheng, M.-N. Rager, Th. Pauporté, Solar Cell. *Sol. RRL* **2020**, 2000348.

[19] T. Zhu, D. Zheng, J. Liu, L. Coolen, Th. Pauporté, *ACS Appl. Mater. Interfaces* **2020**, *12*, 37197−37207.

[20] J. W. Lee, D. H. Kim, H. S. Kim, S. W. Seo, S. M. Cho, N. G. Park, *Adv. Energy Mater.* **2015**, *5*, 1501310.

[21] Y. H. Park, I. Jeong, S. Bae, H. J. Son, P. Lee, J. Lee, C. H. Lee, M. J. Ko, *Adv. Funct. Mater.* **2017**, *27*, 1605988.

[22] Z. M. Li, N. Liu, Z. Liu, X. Wang, Y. D. Hu, Q. F. Xu, S. D. Li, Z. Qiao, L. Cheng, C. W. Wang, K. Meng, G. A. Chen, *Energy Tech.* **2020**, *8*, 2000224.

[23] S. D. Li, Z. Liu, Z. Qiao, X. Wang, L. Cheng, Y. F. Zhai, Q. F. Xu, Z. M. Li, K. G. Meng, Chen, *Adv. Funct. Mater.* **2020**, 2005846.

[24] J. C. Germino, R. Szostak, S. G. Motti, R. F. Moral, P. E. Marchezi, H. S. Seleghini, , L. G. Bonato, F. L. de Araujo, T. D. Z. Atvars, L. M. Herz, D. Fenning, A. Hagfeldt, A. F. Nogueira, *ACS Photonics* **2020**, *7*, 2282-2291.

[25] D. Prochowicz, R. Runjhun, M. M. Tavakoli, P. Yadav, M. Saski, A.Q. Alanazi, D.J. Kubicki, Z. Kaszkur, S. M. Zakeeruddin, J. Lewinski, M. Gratzel, *Chem. Mater.* **2019**, *31*, 1620-1627.

[26] X. X. Gao, W. Luo, Y. Zhang, R. Y. Hu, B. Zhang, A. Zuttel, Y.Q. Feng, M. K. Nazeeruddin, *Adv. Mater.* **2020**, *32*, 1905502.

[27] S. S. Zhang, S. H. Wu, R. Chen, W. T. Chen, Y. Q. Huang, Z. C. Yang, W. Chen, *J. Mater. Chem. C* **2020**, *8*, 1642-1648.

[28] K. Schutt, P. K. Nayak, A. J. Ramadan, B. Wenger, Y. H. Lin, H. J. Snaith, *Adv. Funct. Mater.* **2019**, *29*, 1900466.

[29] H. X. Wang, S. L. Cao, B. Yang, H. Y. Li, M. Wang, X. F. Hu, K. Sun, Z. G. Zang, Solar RRL 4 (2020) 1900363.

[30] M.Y. Yan, T.X. Xiang, X.X. Yu, J.Y. Xiao, W. Li, Z.L. Ku, F.Z. Huang, J. Zhong, Y. Peng, Y.B. Cheng, *Solar RRL* **2020**, *4*, 1900363.

[31] J. Yang, Y. Chen, W. Tang, S. Wang, Q. Ma, Y. Wu, N. Yuan, J. Ding, W.H. Zhnag, *J. Energy Chem.* **2020,** *48*, 217-225.

[32] N. Li, Y. Luo, Z. Chen, X. Niu, X. Zhang, J. Lu, R. Kumar, J. Jiang, H. Liu, X. Guo, B. Lai, G. Brocks, Q. Chen, S. Tao, D.P. Fenning, H. Zhou, *Joule* **2020**, 4, 1743-1758.

[33] X. Zhao, C. Yao, K. Gu, T. Liu, Y. Xia, Y.L. Loo, *Energy Environ. Sci.* **2020**, *13,* 4334-4343.

[34] J. Dagar, K. Hirselandt, A. Merdasa, A. Czudek, R. Munir, F. Zu, N. Koch, T. Dittrich, E. L. Unger, *Solar RRL* **2019**, *3*, 1900088.

[35] W. Chen, Y. C. Zhou, G. C. Chen, Y. H. Wu, B. Tu, F. Z. Liu, L. Huang, A. M. C. Ng, Djurisic, Z. B. He, *Adv. Energy Mater.* **2019**, *9*, 1803872.

[36] N. Zhu, X. Qi, Y. Q. Zhang, G. H. Liu, C. C. Wu, D. Wang, X. Guo, W. Luo, X. D. Li, H. Z. Hu, Z. J. Chen, L.X. Xiao, B. Qu, *ACS Appl. Energy Mater.* **2019**, *2*, 3676-3682.

[37] X. Zheng, Z. Song, Z. Chen, S. S. Bista, P. Gui, N. Shrestha, C. Chen, C. Li, X. Yin, R. A. Awni, H. Lei, C. Tao, R. J. Ellingson, Y. Yan, G. Fang, *J. Mater. Chem. C* **2020**, *8*, 1972-1980.

[38] P. F. Wang, J. Wang, X. Zhang, H. L. Wang, X. L. Cui, S. J. Yuan, H. Lu, L. Tu, Y. Q. Zhan, L. R. Zheng, *J. Mater. Chem. A* **2018**, *6*, 15853-15858.

[39] M. M. U. Zaman, M. Imran, A. Saleem, A. H. Kamboh, M. Arshad, N. A. Khan, P. Akhter, *Physica B* **2017**, *522*, 57–65.

[40] M. Abdi-Jalebi, Z. Andaji-Garmaroudi, S. Cacovich, C. Stavrakas, B. Philippe, J. M. Richter, M. Alsari, E. P. Booker, E. M. Hutter, Pearson, A. J. Lilliu, T. J. Savenije, H. G. RensmoDivitini, C. Ducati, R. H. Friend, S. D. Stranks, *Nature* **2018**, *555*, 497-501.

[41] N. Wang, Y. Zhang, P. Zeng, Y. Hu, F. Li, M. Liu, *J. Appl. Phys.* **2020**, *128*, 044504.

[42] W. S. Yang, J. H. Noh, N. J. Jeon, Y. C. Kim, J. Ryu, S. Seo, S. I. Seok, *Science* **2015**, *348*, 1234-1237.

[43] J.-W. Lee, D.-J. Seol, A.-N. Cho, N.-G. Park, *Adv. Mater.* **2014**, *26*, 4991-4998.

[44] D. Zheng, T. Zhu, Th. Pauporté, *ACS Appl. Energy Mater.* **2020**, *3*, 10349–10361.

[45] H.-S Yoo, N. G. Park, *Sol. Energy Mater. Sol. Cells* **2018**, *179*, 57–65.

[46] J. W. Lee, Z. Dai, T. H. Han, C. Choi, S. Y. Chang, S. J. Lee, N. De Marco, H. Zhao, P. Sun, Y. Huang, Y. Yang, *Nat. Commun.* **2018**, *9*, 3021.

[47] H. Zhu, Y. Liu, F. T. Eickemeyer, L. Pan, D. Ren, M. Ruiz, B. Brian Carlsen, B. Yang, S. Wang, Z. Wang, H. Liu, S. M. Zakeeruddin, A. Hagfeldt, M. Ibrahim Dar, X. Li, M. Grätzel, *Adv. Mater.* **2020**, *32*, 1907757.

[48] M. Kim, G. H. Kim, T. K. Lee, I. W. Choi, H. W. Choi, Y. Jo, Y. J. Yoon, J. W. Kim, J. Lee, D. Huh, S. K. Kwak, J. Y. Kim, D. S. Kim, *Joule* **2019**, *3*, 2179-2192.

[49] L. Cojocaru, S. Uchida, D. Matsubara, H. Matsumoto, K. Ito, Y. Otsu, P. Chapon, J. Nakazaki, T. Kubo, H. Segawa, *Chem. Lett.* **2016**, *45*, 884–886.

[50] Z. Ahmad, M. A. Najeeb, R. A. Shakoor, A. Alashraf, Al-Muhtaseb, S. A. Ahmed Soliman, M. K. Nazeeruddin, *Sci. Rep.* **2017**, *7*,15406.

[51] H. Lee, S. Gaiaschi, P. Chapon, A. Marronnier, H. Lee, J. C. Vanel, D. Tondelier, J.-E. Bourée, Y. Bonnassieux, B. Geffroy, *ACS Energy Lett.* **2017**, *2*, 943−949.

[52] H. Lee, S. Gaiaschi, P. Chapon, D. Tondelier, J.-E. Bourée, Y. Bonnassieux, V. Derycke, B. Geffroy, J*J. Phys. Chem. C* **2019**, *123*, 17728−17734.

[53] H. Yu, H. Lu, F. Xie, S. Zhou, N. Zhao, *Adv. Functional Mater.* **2016**, *26*, 1411-1419.

[54] C. Eames, J. M. Frost, P. R. F. Barnes, B. C. O'Regan, A. Walsh, M. S. Islam, *Nature Commun.* **2015**, *6*, 7497.

[55] J. M. Azpiroz, E. Mosconi, J. Bisquert, F. De Angelis, *Energy Environ. Sci.* **2015**, *8*, 2118-2127.

[56] M. Ulfa, P. Wang, B. Viana, Th. Pauporté, *Proc. SPIE* **2018**, 10533-105332R.

[57] T. Zhu, J. Su, F. Labat, I. Ciofini, Th. Pauporté, *ACS Appl. Mater Interfaces* **2020**, *12*, 744-752.

A co-additive strategy using two chloride compounds in the precursor solution is elaborated to prepare methylammonium-free $Cs_{0.1}MA_{0.9}PbI_3$ layers with outstanding morphological, structural, electrical and optical properties. It results in robust devices which are in hysteresis-free and which deliver a stabilized 20.02% power conversion efficiency.

Daming Zheng, Tao Zhu, Thierry Pauporté*

A Co-Additives Strategy for Blocking Ionic Mobility in Methylammonium-Free Perovskite Solar Cells and High Stability Achievement.